

# Investigation of SMAP Active–Passive Downscaling Algorithms Using Combined Sentinel-1 SAR and SMAP Radiometer Data

Lian He<sup>1</sup>, Yang Hong<sup>1</sup>, Xiaoling Wu<sup>1</sup>, Nan Ye<sup>1</sup>, Jeffrey P. Walker<sup>2</sup>, and Xiaona Chen<sup>1</sup>

**Abstract**—The aim of this paper was to test the capabilities of the Sentinel-1 radar data in downscaling Soil Moisture Active Passive (SMAP) radiometer data for high-resolution soil moisture estimation. Three different active–passive downscaling algorithms, including the brightness temperature-based downscaling algorithm (BTBDA), the soil moisture-based downscaling algorithm (SMBDA), and a change detection method (CDM), were analyzed using pairs of Sentinel-1 active and SMAP passive observations collected over a semiarid landscape in southeastern Australia from May 2015 to May 2016. While these algorithms have been tested previously, this is the first study to evaluate the three algorithms using real Sentinel-1 radar and SMAP radiometer data. The SMAP passive observations were disaggregated to 9-, 3-, and 1-km scales and then compared with ground soil moisture measurements. The results suggest that the root-mean-square error (RMSE) in downscaled soil moisture at 9-km resolution was 0.057, 0.056, and 0.067 cm<sup>3</sup>/cm<sup>3</sup> for the BTBDA, SMBDA, and CDM, respectively. The accuracy of downscaling methods was generally decreased when applied at the finer spatial resolution. The SMBDA had overall better performance in terms of correctly detecting the soil moisture pattern and relatively lower RMSE values, and is, therefore, recommended for the combined Sentinel-1 radar and SMAP radiometer setup for soil moisture monitoring. The influence of incidence angle normalization of Sentinel-1 SAR data on downscaled soil moisture was also investigated and found to be minimal.

**Index Terms**—Active–passive, downscaling algorithm, Sentinel-1, soil moisture, Soil Moisture Active Passive (SMAP).

## I. INTRODUCTION

SOIL moisture is a key variable in controlling the exchange of water and heat energy between the land surface and the atmosphere [1]. Microwave remote sensing has been

Manuscript received October 19, 2017; revised March 15, 2018 and May 7, 2018; accepted May 24, 2018. Date of publication June 21, 2018; date of current version July 20, 2018. This work was supported in part by the National Natural Science Foundation of China under Grant 41701384, Grant 41401375, and Grant 41401426, and in part by the Australian Research Council under Grant DP0984586, Grant LE0453434, and Grant LE0882509. (Corresponding author: Lian He.)

L. He and X. Chen are with the Department of Hydraulic Engineering, Tsinghua University, Beijing 100084, China (e-mail: helian\_2006@126.com; chenxn@mail.bnu.edu.cn).

Y. Hong is with the Institute of Remote Sensing and GIS, Peking University, Beijing 100871, China, with the Department of Hydraulic Engineering, Tsinghua University, Beijing 100084, China, and also with the School of Civil Engineering and Environmental Sciences, The University of Oklahoma, Norman, OK 73019 USA (e-mail: yanghong588@pku.edu.cn).

X. Wu, N. Ye, and J. P. Walker are with the Department of Civil Engineering, Monash University, Clayton, VIC 3800, Australia (e-mail: xiaoling.wu@monash.edu; nan.ye@monash.edu; jeff.walker@monash.edu).

Color versions of one or more of the figures in this paper are available online at <http://ieeexplore.ieee.org>.

Digital Object Identifier 10.1109/TGRS.2018.2842153

widely accepted as the preferred approach to remotely sense the near-surface soil moisture variations at regional and global scales. Several global microwave soil moisture products have been produced with the availability of satellite-based active and passive microwave sensors, such as the Advanced Microwave Scanning Radiometer for the Earth Observing System [2], the Advanced Scatterometer [3], the Soil Moisture and Ocean Salinity mission [4], the Soil Moisture Active Passive (SMAP) mission [5], and the Sentinel-1 mission [6]. Among these active and passive microwave sensors, passive microwave sensors enable accurate soil moisture estimates but with a spatial resolution of several tens of kilometers, which is not sufficient for applications associated with hydrometeorology, hydrology, and agriculture [7]. Therefore, a spatial downscaling to several kilometers or even tens of meters is required for many regional hydrological and agricultural applications.

Many studies have explored the utilization of high-resolution optical/thermal data to spatially disaggregate coarse soil moisture products and a number of downscaling methods have been developed, including the empirical polynomial fitting method [8]–[13], the semiphysical evaporation-based method [14]–[19], and the smoothing filter-based intensity modulation (SFIM) downscaling method [20]–[23]. These methods exploit the relationships that exist between microwave-based soil moisture and optical/thermal-derived estimates of land surface temperature and vegetation indices. Since optical and thermal remote sensing have the advantage of providing land surface parameters at very high spatial resolution, it is possible to obtain disaggregated soil moisture at a spatial resolution much finer than 1 km. However, due to masking of optical/thermal data by cloud, these downscaling approaches are only applicable under clear-sky condition, limiting their application in areas where clouds are frequent [24].

The alternative downscaling approaches are based on a combination of coarse resolution passive microwave data and high-resolution active microwave data. Passive microwave observations show a higher sensitivity to soil moisture than active microwave data, allowing for more accurate estimation over large spatial scales, whereas active microwave observations offer increased spatial detail although the soil moisture retrieval accuracy is more strongly affected by the surface roughness and vegetation [25]. To overcome the individual limitations of each observation type, NASA developed the SMAP mission, which aimed to utilize fine-scale (3 km) active microwave observations to downscale the coarse-scale (36 km)

passive microwave observations to a medium-scale (9 km) resolution [5].

In preparation for the SMAP mission, several active-passive downscaling approaches were proposed. The SMAP baseline downscaling algorithm [26] proposes to downscale low-resolution (36 km) brightness temperature  $T_B$  to an intermediate resolution (9 km) using high-resolution (1 km) radar backscatter  $\sigma^0$ , with the final soil moisture product being retrieved from the downscaled brightness temperature at 9-km spatial resolution. Alternatively, the SMAP optional downscaling approach [27] directly disaggregates 36-km radiometer-based soil moisture with radar backscatter to retrieve the intermediate resolution soil moisture product. A further candidate downscaling approach is based on the change detection method (CDM), using the assumption of an approximately linear dependence of radar backscatter and brightness temperature change on soil moisture change [28]–[30]. Another totally different downscaling approach proposed in [31] downscales radiometer observations using radar measurements through the synergy of the active and passive data in a Bayesian framework. Some of these active-passive downscaling techniques have been evaluated using airborne observations in different regions that present with different surface and land cover conditions [32]–[34].

Unfortunately, SMAP’s L-band radar stopped working on July 7, 2015, which seriously hampers the proposed soil moisture estimation at high resolution. One of the feasible approaches to recover the high-resolution soil moisture capability of the SMAP mission is to substitute the failed SMAP’s L-band radar with the European Space Agency (ESA)’s Sentinel-1 C-band SAR and apply the same proposed active-passive downscaling algorithms [35]. Since the SMAP and Sentinel-1 satellites have similar orbit configuration and the Sentinel-1 SAR could provide co-polarization and cross-polarization observations, the active-passive downscaling methods will be applicable. A few attempts have been made to downscale L-band radiometer data using C-band SAR data. Rüdiger *et al.* [36] synergistically used C-band SAR and L-band radiometer data to achieve a high-resolution (1–2 km) brightness temperature product for soil moisture estimation and found that it was promising for using C-band high-resolution radar data for downscaling of L-band radiometer data. Santi *et al.* [37] attempted to enhance the SMAP radiometer resolution up to the Sentinel-1 radar resolution through the SFIM downscaling method proposed in [20]. Das *et al.* [38] illustrated and discussed the possibility of an SMAP–Sentinel combined product for recovery of the SMAP mission post radar failure, with preliminary results showing great promise.

Despite the promising results, integration of C-band active and L-band passive observations for soil moisture retrieval still needs more comprehensive investigations being applied in practice. The objective of this paper is, therefore, to test the capabilities of the combined Sentinel-1 radar and SMAP radiometer setup for soil moisture monitoring. Three active-passive downscaling algorithms, including the SMAP baseline downscaling method [26], the optional downscaling method [27], and a CDM [28], [30], were analyzed using pairs

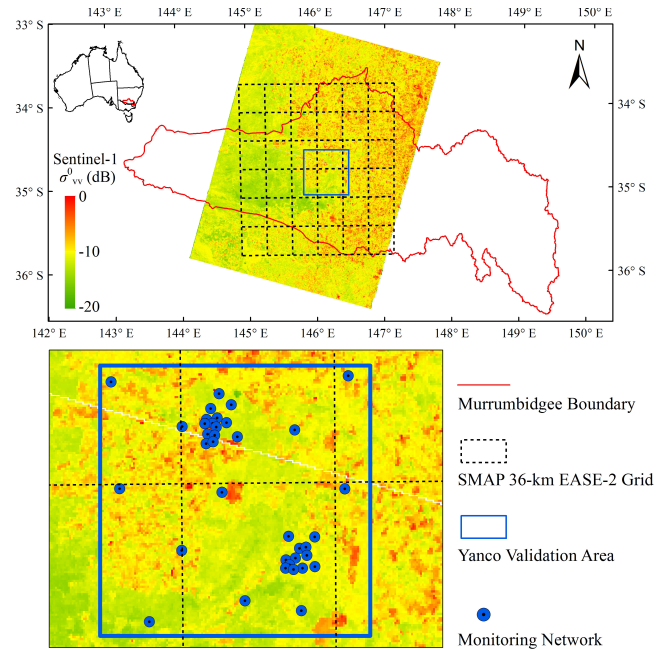


Fig. 1. Overview of the study area, validation area, and regional soil moisture sampling points within the Murrumbidgee river catchment. Sentinel-1 SAR image in VV-polarization acquired on July 28, 2015 of the study region is shown as well and indicates the coverage of Sentinel-1 SAR data. The study area is represented by  $6 \times 6$  36-km EASE-2 grids while the validation area is indicated by square.

of Sentinel-1 active and SMAP passive observations collected over a semiarid landscape in southeastern Australia from May 5, 2015 to May 23, 2016. The SMAP passive observations were downscaled to spatial resolutions of 9, 3, and 1 km using high-resolution Sentinel-1 SAR data, and the accuracy of these products assessed through comparison with ground measurements collected by a network of 75 individual stations located within the Yanco core validation site [39], [40].

## II. STUDY AREA AND DATA SET

### A. Study Area

The study area is located in the Murrumbidgee catchment in southeastern Australia and represented by  $6 \times 6$  S-km EASE-2 (Equal Scalable Earth version 2.0) grids (Fig. 1). Land use in the study area is predominantly agricultural with the exception of some forest areas in the eastern part of the study area [41], [42]. Agricultural land use varies greatly in intensity and includes pastoral, more intensive grazing, broad-acre cropping, and intensive agriculture. An area of approximately 60 km  $\times$  60 km near the township of Yanco (long 146° 10' E, lat 34° 50' S) is selected as the validation area (represented by the solid rectangle in Fig. 1). This region is a flat semiarid agricultural area with elevation changes of only a few meters.

In the Murrumbidgee river catchment, a soil moisture monitoring network has been maintained since September 2001 [41]. Among the monitoring network, 37 stations (indicated by solid points in Fig. 1) located within the Yanco validation area were selected for this study. At each station, near-surface (0–5 cm) and root-zone soil

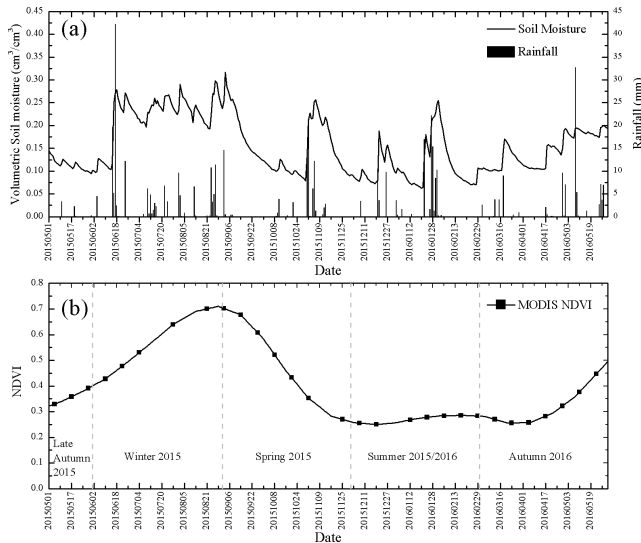


Fig. 2. (a) Averaged daily near-surface (0–5 cm) soil moisture measured across the 37 soil moisture monitoring stations located in the Yanco region, and associated averaged daily rainfall from May 1, 2015 to May 31, 2016. (b) Averaged NDVI obtained from MODIS 16-day synthesized NDVI product (MOD13A2) across the Yanco region from May 1, 2015 to May 31, 2016. Gray dashed lines indicate seasonal separation in Australia.

moisture, soil temperature, and precipitation were measured. In order to characterize the vegetation conditions of the study area, the normalized difference vegetation index (NDVI) was introduced, and the MODIS 16-day synthesized NDVI product (MOD13A2) [43] at 1-km resolution was downloaded from the USGS website for the period from May 1, 2015 to May 31, 2016.

Fig. 2 shows the temporal dynamics of soil moisture and vegetation conditions over the study area from May 1, 2015 to May 31, 2016. In Fig. 2(a), the average soil moisture values calculated from the 37 monitoring stations of soil moisture measurements are presented along with the average daily rainfall amounts. It can be seen that rainfall could directly increase the near-surface soil moisture and a dry-down event could be observed with no rainfall experienced. Each season was composed of multiple complete wetting–drying periods, resulting in large dynamics in soil moisture. Fig. 2(b) displays the time series of the mean NDVI values for the study area. In the growing season (the late autumn and winter of 2015), NDVI increased as vegetation grew and finally reached to a maximum value of about 0.7 at the end of winter. As the vegetation began to mature and dry, NDVI decreased gradually from about 0.7 to 0.3 in the spring of 2015. During the summer and mid-autumn (from September 1, 2015 to April 20, 2016), NDVI fluctuated around 0.3 and exhibited a narrow dynamic range ( $<0.05$ ). After the mid-autumn of 2016, NDVI increased as the vegetation grew and reached to 0.5 at the end of the autumn of 2016.

### B. SMAP Radiometer Data

The SMAP mission [5] was launched on January 31, 2015, and characterized by the unique feature of carrying on board both active radar and passive radiometer instruments at L-band

for simultaneous data acquisition. The SMAP satellite is in a sun-synchronous near-polar orbit at an altitude of 685 km, with a local time of ascending node of 6 P.M. and a revisit time of 2–3 days. Data are collected in 1000-km swaths at a constant incidence angle of 40°.

In this paper, the SMAP Level-1C brightness temperature (L1C\_TB) product and the standard Level 2 Passive Soil Moisture Product (L2\_SM\_P) on the 36-km EASE-2 grid were obtained. In the L2\_SM\_P product, five soil moisture retrieval algorithms are implemented [44] with the single-channel algorithm at vertical polarization (SCA-V) selected as the postlaunch baseline retrieval algorithm for the beta release due to its best overall soil moisture performance metrics [39]. Therefore, the L1C\_TB product at vertical polarization and the L2\_SM\_P product from the SCA-V algorithm were utilized in the following analyses.

### C. Sentinel-1 SAR Data

Sentinel-1, part of the ESA Copernicus program, consists of two satellites (A and B) that were launched on April 3, 2014 and April 22, 2016, respectively. The satellites are in opposite polar sun-synchronous orbits at an altitude of 693 km, with a mean solar local time of the ascending node of 6 P.M. and a repeat cycle of 1–2 weeks. The SAR system operates within C-band (5.405 GHz) frequencies in one of four acquisition modes: stripmap, interferometric wide swath (IW), extra-wide swath, and wave, with IW being the main operational mode over land and coastal areas. Data are collected in 250-km swaths at incidence angles ranging from 29.1° to 46°, providing a ground resolution of 5 m  $\times$  20 m (range  $\times$  azimuth).

In this paper, Level-1 multilooked ground range detected Sentinel-1 data collected in IW mode were used. The Sentinel-1A SAR data acquired over the study area consist of seven descending IW images in dual polarizations (VV and VH) with a mean temporal resolution of about 14 days for the study area from May 5, 2015 to May 23, 2016. These data were radiometrically calibrated, terrain corrected, and normalized to 40° using the cosine correction [45]. To downscale the coarse soil moisture, the Sentinel-1 SAR data were finally aggregated (in power units) from their native resolution to the 1-km EASE-2 grid.

The Sentinel-1 SAR data are appealing for combining with the SMAP radiometer data in two ways [38]: 1) the two satellites have a similar orbit configuration which allows overlapping of their swaths with minimal time difference and 2) the main acquisition mode of Sentinel-1 could provide dual-polarized (VV/VH or HH/HV) observations. Both are key to the SMAP active–passive downscaling algorithms. However, the Sentinel-1 and SMAP satellites were not designed to have synchronized overpasses, so the closest overpass time to the SMAP acquisitions was chosen with the aid of precipitation data. In the case of significant precipitation events, the closest date without precipitation interference was chosen. A total of 28 pairs of Sentinel-1 SAR and SMAP radiometer data were collected over the study region and are listed in Table I. Of the 28 data pairs, 13 pairs were acquired at the same day with time gap between the two acquisitions

TABLE I  
LIST OF SENTINEL-1 SAR DATA AND SMAP RADIOMETER DATA USED IN THIS PAPER

Season	Day	Sentinel-1 Acquisition Date and UTC Time	SMAP Radiometer Acquisition Date and UTC Time	Season	Day	Sentinel-1 Acquisition Date and UTC Time	SMAP Radiometer Acquisition Date and UTC Time
Autumn	1	05/05/2015 19:31	05/05/2015 19:09	Summer	15	07/12/2015 19:31	07/12/2015 19:09
	2	17/05/2015 19:32	16/05/2015 19:21		16	19/12/2015 19:31	18/12/2015 19:21
	3	29/05/2015 19:31	29/05/2015 19:09		17	12/01/2016 19:31	11/01/2016 19:20
Winter	4	10/06/2015 19:31	09/06/2015 19:21		18	24/01/2016 19:31	24/01/2016 19:08
	5	22/06/2015 19:31	22/06/2015 19:09		19	05/02/2016 19:31	04/02/2016 19:21
	6	04/07/2015 19:31	03/07/2015 19:21		20	17/02/2016 19:31	17/02/2016 19:09
	7	28/07/2015 19:31	27/07/2015 19:20		21	29/02/2016 19:31	28/02/2016 19:21
	8	21/08/2015 19:31	22/08/2015 18:56		22	12/03/2016 19:31	12/03/2016 19:09
Spring	9	02/09/2015 19:31	02/09/2015 19:09		Autumn	23	24/03/2016 19:31
	10	14/09/2015 19:31	13/09/2015 19:21	24		05/04/2016 19:31	05/04/2016 19:09
	11	26/09/2015 19:31	26/09/2015 19:09	25		17/04/2016 19:31	18/04/2016 18:57
	12	08/10/2015 19:32	07/10/2015 19:22	26		29/04/2016 19:31	29/04/2016 19:09
	13	20/10/2015 19:32	20/10/2015 19:10	27		11/05/2016 19:31	10/05/2016 19:21
	14	25/11/2015 19:31	24/11/2015 19:22	28		23/05/2016 19:31	23/05/2016 19:08

less than 1 h. For the other 15 pairs, the time gaps were around 24 h. During these time gaps, no rainfall was recorded according to the precipitation data.

### III. METHODOLOGY

#### A. Downscaling Algorithms

Several approaches have been proposed for downscaling the coarse resolution passive microwave-based soil moisture products through combination with high-resolution active microwave observations. In this paper, three active-passive downscaling algorithms were analyzed, including the brightness temperature-based downscaling algorithm (BTBDA) (the SMAP baseline downscaling algorithm) [26], the soil moisture-based downscaling algorithm (SMBDA) (the SMAP optional downscaling algorithm) [27], and a CDM [28], [30]. This section provides a brief summary of each downscaling method.

1) *Brightness Temperature-Based Downscaling Algorithm:* The SMAP active-passive baseline downscaling algorithm first disaggregates the brightness temperature at coarse resolution  $C$  to fine resolution  $F$  by radar backscatter, and subsequently converts the downscaled brightness temperature to soil moisture, and thereby it is referred to as the BTBDA. This method is based on the assumption of a near-linear relationship between radar backscatter ( $\sigma_{pp}^0$ ) and brightness temperature ( $T_{Bp}$ ) at different scales [26], [44]

$$T_{Bp}(C) = \alpha_1(C) + \beta_1(C) \cdot \sigma_{pp}^0(C) \quad (1)$$

$$T_{Bp}(F_j) = \alpha_1(F_j) + \beta_1(F_j) \cdot \sigma_{pp}^0(F_j) \quad (2)$$

where p indicates the polarization (h- or v-polarization), pp represents co-polarization of radar observations  $\sigma^0$  (hh or vv),  $C$  represents coarse scale (36 km),  $F$  represents fine scale (9, 3, or 1 km),  $\alpha_1$  and  $\beta_1$  are the intercept and slope of the linear regression between radar backscatter ( $\sigma_{pp}^0$ ) and brightness temperature ( $T_{Bp}$ ), respectively,  $T_{Bp}(F_j)$  is the brightness temperature value of a particular pixel “ $j$ ” of resolution  $F$ , and  $\sigma^0(F_j)$  is the corresponding radar backscatter

value of pixel “ $j$ .” The radar backscatter value  $\sigma_{pp}^0(C)$  (in the unit of dB) at coarse scale can be obtained by aggregating high-resolution Sentinel-1 SAR data (in power units) within the coarse footprint  $C$ .

By subtracting (1) from (2), the disaggregated brightness temperature  $T_{Bp}(F_j)$  at fine scale  $F$  can be rewritten as [26], [44]

$$T_{Bp}(F_j) = T_{Bp}(C) + \beta_1(C) \cdot [\sigma_{pp}^0(F_j) - \sigma_{pp}^0(C)] + \{[\alpha_1(F_j) - \alpha_1(C)] + [\beta_1(F_j) - \beta_1(C)] \cdot \sigma_{pp}^0(F_j)\}. \quad (3)$$

There are three terms on the right-hand side of (3). The first term  $T_{Bp}(C)$  is the radiometer-measured brightness temperature at coarse scale  $C$ . The second term  $\{\beta_1(C) \cdot [\sigma_{pp}^0(F_j) - \sigma_{pp}^0(C)]\}$  can be calculated based on the regression parameter  $\beta_1(C)$  that is estimated through the time series of radiometer brightness temperature measurements and SAR measurements aggregated to scale  $C$ . The third term  $\{[\alpha_1(F_j) - \alpha_1(C)] + [\beta_1(F_j) - \beta_1(C)] \cdot \sigma_{pp}^0(F_j)\}$  accounts for the deviations of  $\alpha_1$  and  $\beta_1$  within the grid cell  $C$ . This term is in units of brightness temperature and represents the subgrid scale heterogeneity effects.

Since the cross-polarization radar backscatter measurements at fine resolution  $F$  are principally sensitive to vegetation and surface roughness, the subgrid heterogeneity in vegetation and surface characteristics within resolution  $C$  can be captured as  $[\sigma_{pq}^0(C) - \sigma_{pq}^0(F_j)]$ , where pq represents vh- or hv-polarization, i.e., the cross-polarization backscatter at scale  $F_j$  deviations from its coarse-scale aggregate. This heterogeneity indicator  $[\sigma_{pq}^0(C) - \sigma_{pq}^0(F_j)]$  can be further converted to variations in co-polarization backscatter by multiplying a sensitivity parameter  $\Gamma$ , which is defined as  $\Gamma = [\delta\sigma_{pp}^0(F_j)/\delta\sigma_{pq}^0(F_j)]_C$  for each particular grid cell  $C$ . The term  $\Gamma \cdot [\sigma_{pq}^0(C) - \sigma_{pq}^0(F_j)]$  is the projection of the variations due to the heterogeneity in  $\alpha_1$  and  $\beta_1$  in the SAR co-polarization space, and it can be converted to brightness temperature units through multiplication by  $\beta_1(C)$  in (3). Therefore, the third term

$\{\alpha_1(F_j) - \alpha_1(C)\} + \{\beta_1(F_j) - \beta_1(C)\} \cdot \sigma_{pp}^0(F_j)$  on the right-hand side of (3) can be approximated as [26], [44]

$$\begin{aligned} & \{\alpha_1(F_j) - \alpha_1(C)\} + \{\beta_1(F_j) - \beta_1(C)\} \cdot \sigma_{pp}^0(F_j) \\ & \approx \beta_1(C) \cdot \Gamma \cdot [\sigma_{pq}^0(C) - \sigma_{pq}^0(F_j)]. \quad (4) \end{aligned}$$

By combining (3) and (4), the disaggregated brightness temperature at fine resolution  $F$  can be written more compactly as [26], [44]

$$\begin{aligned} T_{Bp}(F_j) = T_{Bp}(C) + \beta_1(C) \cdot \{ & [\sigma_{pp}^0(F_j) - \sigma_{pp}^0(C)] \\ & + \Gamma \cdot [\sigma_{pq}^0(C) - \sigma_{pq}^0(F_j)] \}. \quad (5) \end{aligned}$$

$\beta_1(C)$  (in the unit of K/dB) can be obtained through a linear regression of the time series of  $T_{Bp}(C)$  and  $\sigma_{pp}^0(C)$ . This parameter depends on vegetation cover and type as well as surface roughness, and a moving window of  $\beta$  estimation should be adopted when applying this algorithm to a long time period [26], [46], [47]. One of the assumptions by performing a time regression is that the soil roughness and vegetation conditions do not change greatly over a specified temporal window [48].  $\Gamma$  is a sensitivity parameter for each particular grid cell  $C$  and season defined as  $\Gamma = [\delta\sigma_{pp}^0(F_j)/\delta\sigma_{pq}^0(F_j)]C$ . It can be estimated using high-resolution  $\sigma_{pp}^0(F)$  and  $\sigma_{pq}^0(F)$  measurements through statistical regression. The term  $\Gamma \cdot [\sigma_{pp}^0(C) - \sigma_{pq}^0(F_j)]$  is used to capture the subgrid heterogeneity of vegetation/surface characteristics within grid cell  $C$  [26], [44].

The downscaled brightness temperature  $T_{Bp}(F_j)$  at fine scale is an intermediate product that is then converted to soil moisture using the SCA in conjunction with high-resolution ancillary data [44], [49], which can be expressed as

$$\theta(F_j) = SCA(T_{Bp}(F_j)) \quad (6)$$

where  $\theta(F_j)$  indicates the retrieved soil moisture for a particular pixel “ $j$ ” at fine scale, and  $T_{Bp}(F_j)$  is the corresponding downscaled brightness temperature of pixel “ $j$ ”; SCA is the single-channel soil moisture retrieval algorithm as described in [44] and [49].

The SCA can be applied to brightness temperature  $T_B$  at both vertical and horizontal polarizations. For the SMAP mission, it was found that the SCA-V yielded the best overall soil moisture performance metrics [39] and is selected as the postlaunch baseline retrieval algorithm. Therefore, only the SMAP brightness temperature  $T_B$  at vertical polarization is tested in this paper.

2) *Soil Moisture-Based Downscaling Algorithm*: The optional downscaling algorithm [27] for SMAP mission directly disaggregates the coarse soil moisture  $\theta(C)$  estimated from coarse passive radiometer data by active microwave data. Therefore, it is referred to as the SMBDA. This method utilizes the near-linear relationship between radar backscatter  $\sigma^0$  and volumetric soil moisture  $\theta$  (rather than brightness temperature  $T_B$ ). Derivation and implementation of the SMBDA is similar to that of the BTBDA, but uses the soil moisture  $\theta$  instead of brightness temperature  $T_{Bp}$  in (5). The downscaled soil moisture can be obtained by

$$\begin{aligned} \theta(F_j) = \theta(C) + \beta_2(C) \cdot \{ & [\sigma_{pp}^0(F_j) - \sigma_{pp}^0(C)] \\ & + \Gamma \cdot [\sigma_{pq}^0(C) - \sigma_{pq}^0(F_j)] \} \quad (7) \end{aligned}$$

where  $\theta(F_j)$  is the downscaled soil moisture of a particular pixel “ $j$ ” of fine resolution  $F$ ,  $\theta(C)$  is the radiometer-based soil moisture at coarse resolution  $C$ ,  $\beta_2(C)$  (in the unit of  $\text{cm}^3/\text{cm}^3/\text{dB}$ ) can be obtained through a linear regression of the time series of  $\theta(C)$  and  $\sigma_{pp}^0(C)$  and is also assumed to be time invariant and homogenous over the entire 36-km pixel, and  $\Gamma$  is the same to that in the baseline algorithm.

The SMBDA is similar to the BTBDA. However, the SMBDA does not require high-resolution ancillary data, such as ground temperature and vegetation water content (VWC), which are necessary for soil moisture inversion and usually difficult to obtain. This would be an advantage of the SMBDA over the BTBDA.

3) *Change Detection Method*: The CDM assumes a linear relationship between the temporal change of radar backscatter and temporal change of soil moisture at the same spatial scale. This method uses the previous radiometer-scale soil moisture retrieval updated with the moisture change evident in the higher resolution radar backscatter change as [30]

$$\begin{aligned} \theta(F_j, t) = \theta(C, t - t_R) \\ + \beta_3(C) \cdot [\sigma_{pp}^0(F_j, t) - \sigma_{pp}^0(F_j, t - t_R)] \quad (8) \end{aligned}$$

where  $\theta(F_j, t)$  is the soil moisture of a particular pixel “ $j$ ” of resolution  $F$  acquired at time  $t$ ,  $\theta(C, t - t_R)$  is the soil moisture of resolution  $C$  acquired at time  $t - t_R$ ,  $t_R$  is the revisit time of the observations, and  $\beta_3(C)$  (in the unit of  $\text{cm}^3/\text{cm}^3/\text{dB}$ ) is also the sensitivity of volumetric soil moisture  $\theta$  to radar backscatter  $\sigma^0$ , and can be obtained through the time series of  $\theta(C)$  and  $\sigma_{pp}^0(C)$ .

### B. Incidence Angle Normalization of Sentinel-1 SAR data

Sentinel-1 IW data are collected at incidence angles ranging from  $29.1^\circ$  to  $46^\circ$  [6]. This angular variability would induce radar backscatter differences [50], which may be corrected by normalizing the backscatter observations with respect to a reference incidence angle. Several approaches have been developed for incidence angle normalization [45], [50], [51]. One of the most often used techniques is cosine correction, which was based on Lambert’s law for optics and initially introduced by [52]. The measured radar backscatter  $\sigma_{\theta_i}^0$  at an incidence angle  $\theta_i$  can be normalized toward a reference angle  $\theta_{\text{ref}}$  according to [45]

$$\sigma_{\text{ref}}^0 = \frac{\sigma_{\theta_i}^0 \cos^n(\theta_{\text{ref}})}{\cos^n(\theta_i)} \quad (9)$$

where  $\sigma_{\text{ref}}^0$  is the backscatter normalized to a reference angle  $\theta_{\text{ref}}$ , and  $n$  is the power index characterizing the type of scattering mechanism and ultimately the land cover characteristics [53], [54] with values of  $n = 1$  or  $n = 2$  often applied.

Previous research has shown that the theoretical assignment of  $n = 1$  and  $n = 2$  applies when the target area behaves as or approaches the behavior of a volume scatterer. It was found that the best  $n$  values varied between 0.2 and 3.4 depending on vegetation type and season for L-band HH polarization data [50]. In the following analyses, the Sentinel-1  $\sigma^0$  normalized with  $n = 2$  was employed and

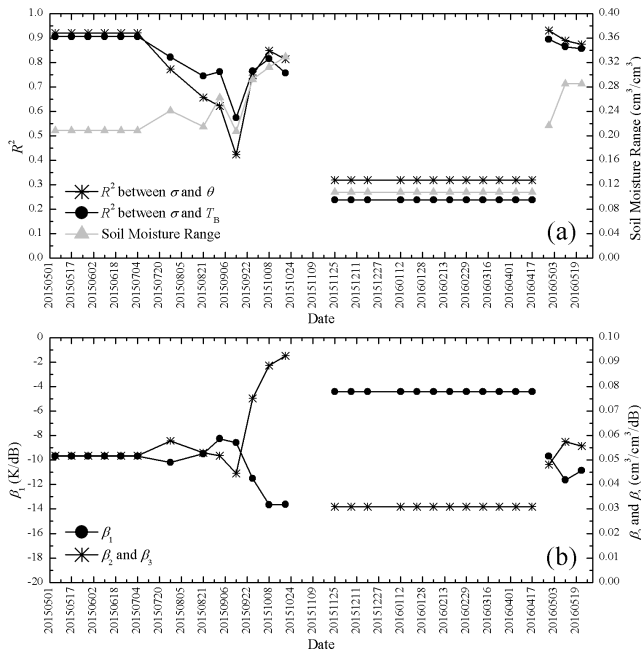


Fig. 3. Time series of (a) average correlation  $R^2$  across the whole study area at all days for the three downscaling algorithms along with the average soil moisture dynamic ranges within the temporal window, and (b) average  $\beta$  across the whole study area for  $\beta_1$  of the BTBDA and  $\beta_2$  and  $\beta_3$  of the SMBDA and the CDM.

the impact of the power index  $n$  on the soil moisture retrievals was discussed.

#### IV. RESULTS AND DISCUSSION

##### A. Estimation of $\beta$

In order to estimate  $\beta$  of each downscaling scheme, the radar observations from Sentinel-1 SAR data on 1-km EASE-2 grids were spatially aggregated (in power units) to 36 km and compared with the SMAP radiometer brightness temperature  $T_B$  or the SMAP radiometer-based soil moisture  $\theta$ . For a particular pixel at 36-km resolution,  $\beta$  was determined as the slope of the linear equation fit to a time series of  $\sigma^0$  and  $T_B$  or  $\theta$ . For the BTBDA,  $\beta_1$  was estimated from  $\sigma^0$  and  $T_B$ , while for the SMBDA and the CDM,  $\beta_2$  and  $\beta_3$  were estimated from  $\sigma^0$  and  $\theta$ . Since both  $\beta_2$  and  $\beta_3$  represent the sensitivity of soil moisture  $\theta$  to radar backscatter  $\sigma^0$ , the same value was used.

As  $\beta$  was estimated from time series of  $\sigma^0$  and  $T_B$  or  $\theta$  at 36 km, it is expected that using more data pairs would attribute to a more accurate linear regression so as to make it statistically significant. However, more date would require a longer window that could also introduce error due the change of land cover condition. Since  $\beta$  varies over time due to change in soil and vegetation conditions [26], [32], [47], a moving window of  $\beta$  estimation should be adopted when applying the downscaling algorithms to a long time period.

In this paper, the length of data window was determined according to the NDVI values [Fig. 2(b)]. More specifically, during the periods of day 1–day 14 and day 26–day 28 when the NDVI changed rapidly over time, a moving window was used with the number of data window set as 6, resulting

in a length of temporal window about two months. For the period of day 15–day 25, the NDVI value fluctuated around 0.3 and exhibited a narrow dynamic range, indicating that the vegetation condition remained almost unchanged. Therefore, this period was treated separately and the length of data window was set as 11.

Fig. 3 displays the time series of average correlation  $R^2$  and  $\beta$  across the whole study area for the three downscaling algorithms. The soil moisture dynamic range defined as the difference between the largest and the smallest soil moisture values within a moving window was also calculated and displayed. In Fig. 3(a), it can be seen that in most cases the correlation  $R^2$  between  $\sigma^0$  and  $T_B$  or  $\theta$  was high with some exceptions. During the periods of day 1–day 14 and day 26–day 28 when the soil moisture dynamic range was above  $0.20 \text{ cm}^3/\text{cm}^3$ , the  $R^2$  values were high with average values of 0.80 and 0.77, respectively, for the BTBDA and SMBDA/CDM. The high  $R^2$  values confirm the fidelity of the linear functional relationship between  $\sigma^0$  and  $T_B$  or  $\theta$ , indicating that the Sentinel-1 SAR data show great potential in downscaling the L-band  $T_B$  or soil moisture  $\theta$ . However, relatively low correlation  $R^2$  values were found from day 15 to day 25, when the  $R^2$  values were about 0.24 and 0.32, respectively, for the BTBDA and SMBDA/CDM. Reasons for this could be associated with relatively low dynamic range in soil moisture (about  $0.10 \text{ cm}^3/\text{cm}^3$ ), which agrees well with the finding in [26].

Fig. 3(b) illustrates the variations of  $\beta$  over time. The observed sensitivity of brightness temperature or soil moisture to radar backscatter was much higher than that obtained in previous studies. For example,  $\beta_1$  from BTBDA varied from  $-14$  to  $-4$  K/dB, and its magnitude was generally larger than that of previous studies obtained at L-band (from  $-8$  to  $0$  K/dB) [26], [32], [33], [46]. Meanwhile,  $\beta_2/\beta_3$  from SMBDA and CDM ranged from  $0.031$  to  $0.093 \text{ cm}^3/\text{cm}^3/\text{dB}$ , being much higher than that of previous study obtained at L-band (from  $0.0293$  to  $0.0332 \text{ cm}^3/\text{cm}^3/\text{dB}$ ) [54]. Reasons for these are more related to the relatively large dynamic range of soil moisture [see Fig. 3(a)] within each data window.

Previous studies have demonstrated that  $\beta$  is dependent on soil and vegetation conditions [26], [32], [47]. Fig. 3 illustrates that the dependence of  $\beta$  on soil and vegetation conditions varied over time. From day 6 to day 9, the soil moisture dynamic range remained relatively stable and around 0.23. During this period,  $\beta_1$  increased and  $\beta_2/\beta_3$  decreased as the NDVI increased rapidly since the dense vegetation cover could mask the brightness temperature or soil moisture sensitivity of radar measurements [55]. During the period of day 10–day 13, the NDVI decreased gradually as the vegetation began to mature and dry [see Fig. 2(b)] and the surface scattering was expected to increase. Therefore,  $\beta_1$  decreased and  $\beta_2/\beta_3$  increased as the soil moisture dynamic range increased from  $0.20$  to  $0.35 \text{ cm}^3/\text{cm}^3$  [see Fig. 3(a)]. The dependence of  $\beta$  on soil moisture dynamic range can also help to explain the decrease in  $\beta_1$  and the increase in  $\beta_2/\beta_3$  from day 26 to day 28. During the period of day 15–day 25, the NDVI was relatively low and the sensitivities of brightness temperature or soil moisture sensitivity to radar backscatter were expected to be

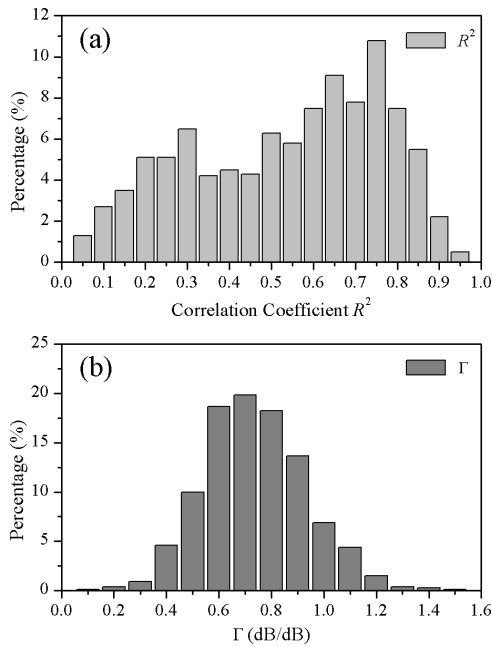


Fig. 4. Histogram of (a) correlation coefficient  $R^2$  values between  $\sigma_{vv}^0$  and  $\sigma_{vh}^0$  and (b)  $\Gamma$  values obtained over the whole study area for all acquisition dates.

high (i.e., low  $\beta_1$  value and high  $\beta_2/\beta_3$  value). However, since the soil moisture dynamic range was relatively low, the sensitivities were not high.

### B. Estimation of $\Gamma$

For the BTBDA and the SMBDA,  $\Gamma$  defined as the sensitivity of radar co-polarization  $\sigma_{vv}^0$  to cross-polarization  $\sigma_{vh}^0$  needed to be calculated. The  $\Gamma$  parameter represents the subgrid scale heterogeneity effects [26]. For each 36-km grid, the value of  $\Gamma$  was calculated using the snapshots of all  $\sigma_{vv}^0 - \sigma_{vh}^0$  pairs at 1-km resolution contained within each 36-km grid.

Fig. 4 displays the histograms of correlation  $R^2$  values between  $\sigma_{vv}^0$  and  $\sigma_{vh}^0$ , and  $\Gamma$  values obtained over the whole study area for all days. The mean value of correlation  $R^2$  is about 0.54, and about 75% pixels have correlation  $R^2$  values greater than 0.40, indicating that the co- and cross-polarizations are strongly correlated. Consequently,  $\Gamma$  can be accurately estimated. The obtained  $\Gamma$  values mostly range between 0.50 and 0.90 with a mean value of about 0.74 and a standard deviation value of about 0.20, which is in good agreement with the results presented in [26] and [33].

Fig. 5 displays the time series of the mean and standard deviation values of  $\Gamma$  calculated over the whole study area for all acquisition dates. The mean value of  $\Gamma$  varies according to different seasons and shows a positive correlation with NDVI [see Fig. 2(b)] with a correlation  $R^2$  value of being about 0.51. There was a slight upward trend in mean  $\Gamma$  value in the late autumn and winter period of 2015 (day 1–day 8) as the NDVI value increased continuously from 0.3 to 0.7 [see Fig. 2(b)], and a clear downward trend during the spring of 2015 (day 9–day 14) as the NDVI value gradually

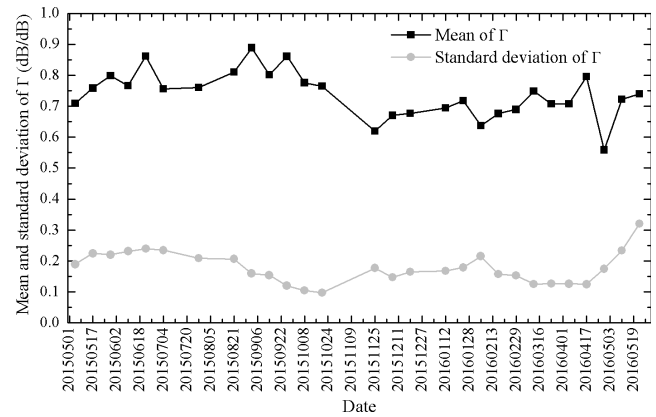


Fig. 5. Time series of mean and standard deviation of  $\Gamma$  calculated from 36 pixels over the whole study area.

decreased from 0.7 to 0.3 [see Fig. 2(b)]. This is likely associated with changes in vegetation conditions. High NDVI values may result in an increase in volume scattering, and thus an increase in cross-polarized radar backscatter  $\sigma_{vv}^0$ . Meanwhile, the radar cross-polarization  $\sigma_{vh}^0$  measurements are very sensitive to the vegetation information since the surface backscattering does not generate significant cross-polarization signal [56]. Therefore, increased NDVI leads to higher volume scattering and hence higher  $\Gamma$  values, and vice versa, which is in good agreement with the results presented in [26] and [33]. In summer season (day 15–day 21), the NDVI was stable and around 0.27, and the  $\Gamma$  fluctuated slightly around 0.68. During the autumn of 2016 (day 22–day 28), the  $\Gamma$  fluctuated a lot and no obvious trend was observed in  $\Gamma$  value even the NDVI demonstrated an obvious increase. More specifically, the  $\Gamma$  dropped from 0.80 to 0.55 from day 25 to day 26 without the NDVI increased a lot. This may be caused by the changes in the soil conditions due to rainfalls or soil tillage.

The standard deviation of  $\Gamma$  value at each day was fairly large and may be caused by the heterogeneity within the whole study area. Since the study area was covered by several land types (i.e., cropland, pasture, and forest), the large standard deviation was more associated with variations in land cover. Moreover, rainfall could change the soil roughness and vegetation conditions, which could also change the heterogeneity within the study area, particularly when it did not rain each time over the whole domain [47].

### C. Soil Moisture Maps

The soil moisture downscaling results for the BTBDA, SMBDA, and CDM are presented in Fig. 6 on June 9, 2015 and in Fig. 7 on July 27, 2015 as examples of dry and wet conditions, respectively. Pixels outside the coverage area of Sentinel-1 SAR data or having missing values caused by the failure of retrieval algorithm appear white. In this paper, the typical range of volumetric soil moisture was set as from 0.02 to 0.60  $\text{cm}^3/\text{cm}^3$ . The downscaling algorithms would fail if the estimated soil moisture value fell outside this typical range. Moreover, for the BTBDA, it requires high-resolution ancillary data, such as soil temperature, soil texture, and VWC.

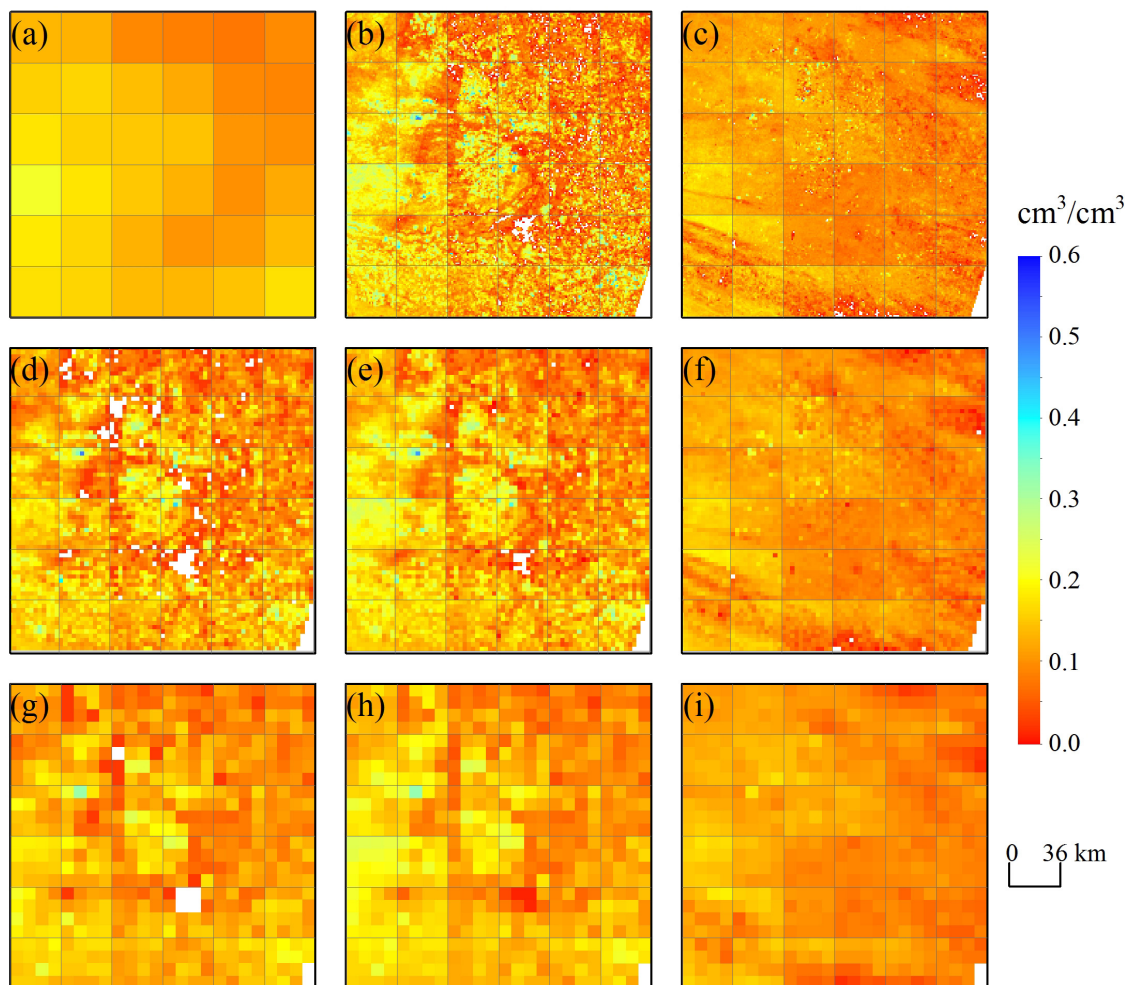


Fig. 6. Example of soil moisture maps on June 9, 2015. (a) S-km radiometer-based soil moisture. (b) and (c) Downscaled soil moisture at 1-km resolution for SMBDA and CDM. (d)–(f) Downscaled soil moisture at 3-km resolution for BTBDA, SMBDA, and CDM. (g)–(i) Downscaled soil moisture at 9-km resolution for BTBDA, SMBDA, and CDM. The S-km EASE-2 grids are also outlined by gray lines.

Therefore, errors in these ancillary data may accumulate through the inversion model [44], [49] and may lead to the failure of this method. Due to the lack of 1-km resolution ancillary data, soil moisture maps were not available at 1-km resolution for the BTBDA. To evaluate the spatial distribution of the downscaled soil moisture, the SMAP radiometer-based soil moisture at 36 km is also displayed.

In terms of comparison among different downscaling algorithms, the three approaches yielded quite different results. The CDM demonstrated much less spatial heterogeneity within each 36-km grid cell when compared to the BTBDA and SMBDA. In addition, the CDM failed to capture the wet conditions on July 27, 2015, in the bottom right area of the study area where soil moisture values from this method were about  $0.30 \text{ cm}^3/\text{cm}^3$ , significantly lower than that from the S-km soil moisture product (about  $0.40 \text{ cm}^3/\text{cm}^3$ ). This failure is probably due to the dense vegetation over the bottom right area where the NDVI value was about 0.75. A close look into the radar and soil moisture measurements shows that the radar backscatter remained almost unchanged while the soil moisture increased from about 0.30 to around  $0.40 \text{ cm}^3/\text{cm}^3$

from day 6 to day 7, indicating that the radar backscatter sensitivity to soil moisture has been attenuated by the dense vegetation. Conversely, both BTBDA and SMBDA were able to effectively capture the dry and wet soil moisture conditions observed by the S-km soil moisture product and reproduced them at the higher spatial resolutions of 1, 3, and 9 km. Soil moisture maps from the BTBDA and SMBDA showed a similar spatial pattern. However, the SMBDA appeared to be better correlated with the S-km soil moisture product over the entire study area, which is due to the fact that the downscaling method relies on the passive microwave soil moisture product as benchmark.

It can also be observed that soil moisture from the BTBDA appeared to be more scattered within the Sentinel-1 data coverage, especially at dry conditions [Fig. 6(d) and (e)]. In contrast, the SMBDA and the CDM could obtain more spatially complete soil moisture maps, with a very small numbers of pixels having missing values due to the failure of retrieval algorithm. Hence, the spatially complete soil moisture map appears to be an advantage of the SMBDA over the BTBDA.

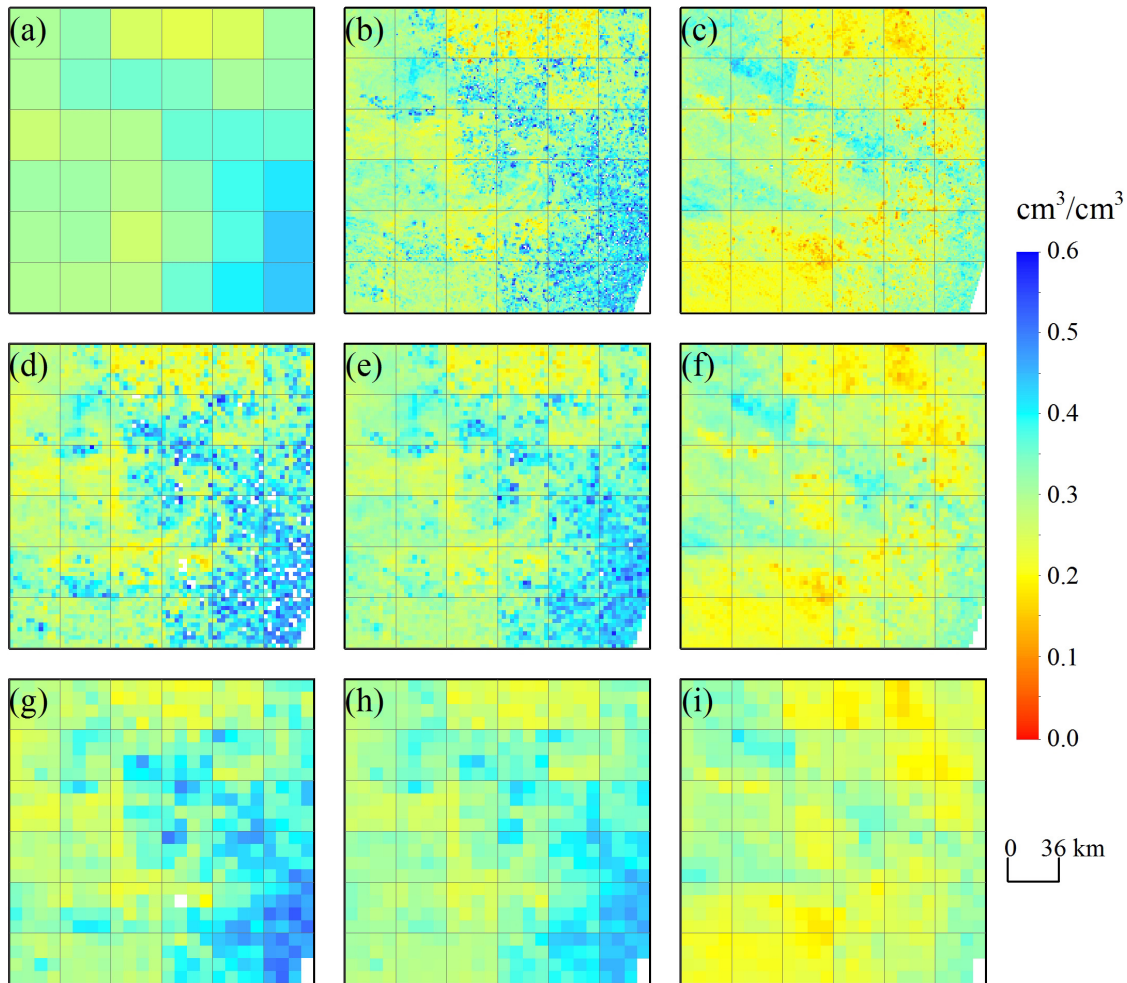


Fig. 7. Example of soil moisture maps on July 27, 2015. (a) S-km radiometer-based soil moisture. (b) and (c) Downscaled soil moisture at 1-km resolution for SMBDA and CDM. (d)–(f) Downscaled soil moisture at 3-km resolution for BTBDA, SMBDA, and CDM. (g)–(i) Downscaled soil moisture at 9-km resolution for BTBDA, SMBDA, and CDM. The S-km EASE-2 grids are also outlined by gray lines.

#### D. Validation of Soil Moisture Retrievals in Yanco Area

The soil moisture retrievals from the SMAP radiometer-based soil moisture product and the three downscaling algorithms were evaluated using ground measurements in the Yanco area, as shown in Fig. 1 at four spatial scales (i.e., 36, 9, 3, and 1 km). The satellite products were compared with soil moisture values obtained through averaging the measurements of all stations within a grid cell. Only the grid cells with a sufficient number of ground measurements are selected for validation. The threshold number of ground soil moisture measurements within a pixel was set as 8, 3, 2, and 1, respectively, for 36-, 9-, 3-, and 1-km spatial scales. From the matchups, the bias, coefficient of determination ( $R^2$ ), root-mean-square error (RMSE), and unbiased root-mean-square error (ubRMSE) were calculated and are listed in Table II, while Fig. 8 shows the scatterplots of soil moisture retrievals compared with ground measurements.

For the SMAP radiometer-based soil moisture product at 36 km, overall good agreement was found between ground measurements and satellite products. The satellite products were highly correlated with the ground measurements with  $R^2$  value being 0.85. A positive bias of  $0.013 \text{ cm}^3/\text{cm}^3$  was observed, indicating slightly higher values for the retrieved

TABLE II  
STATISTICS COMPUTED BETWEEN THE RETRIEVED AND GROUND MEASURED SOIL MOISTURE AT 36-, 9-, 3- AND 1-km RESOLUTIONS;  $N$  IS THE NUMBER OF SAMPLES. THESE RESULTS ARE OBTAINED WITH  $\Gamma \neq 0$

Scale	Method*	RMSE ( $\text{cm}^3/\text{cm}^3$ )	Bias ( $\text{cm}^3/\text{cm}^3$ )	ubRMSE ( $\text{cm}^3/\text{cm}^3$ )	$R^2$	$N$
36-km	SMAP passive	0.048	0.013	0.047	0.85	53
	BTBDA	0.057	0.002	0.057	0.77	150
9-km	SMBDA	0.056	0.003	0.056	0.76	151
	CDM	0.067	0.013	0.066	0.60	148
	BTBDA	0.074	0.011	0.073	0.63	178
3-km	SMBDA	0.072	0.008	0.072	0.60	179
	CDM	0.080	0.012	0.079	0.50	174
	BTBDA	-	-	-	-	-
1-km	SMBDA	0.092	0.010	0.091	0.44	900
	CDM	0.100	0.013	0.098	0.31	872

\*: BTBDA, SMBDA, and CDM represent the Brightness Temperature Based Downscaling Algorithm, the Soil Moisture Based Downscaling Algorithm, and the Change Detection Method, respectively. “-”: Data not available due to the lack of 1-km resolution ancillary data for the BTBDA.

than the measured soil moisture. The ubRMSE value was about  $0.047 \text{ cm}^3/\text{cm}^3$ , which is close to the target accuracy of the SMAP products of  $0.040 \text{ m}^3/\text{m}^3$ . While these results

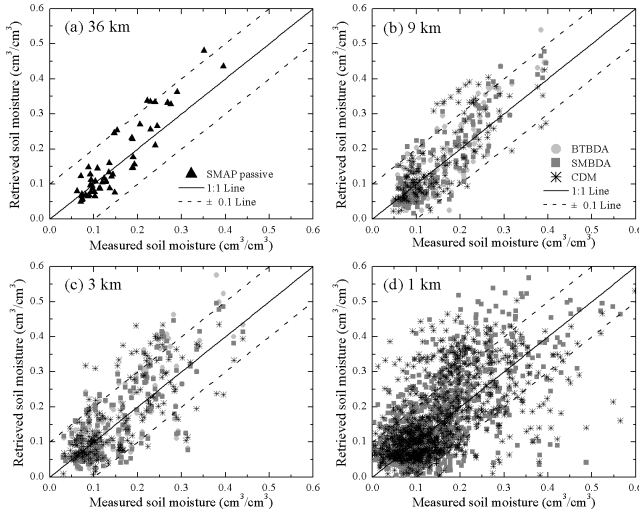


Fig. 8. Scatterplots of retrieved and measured soil moisture values at (a) 36-, (b) 9-, (c) 3-, and (d) 1-km scales. BTBDA, SMBDA, and CDM represent the brightness temperature-based downscaling algorithm, the soil moisture-based downscaling algorithm, and the change detection method, respectively.

were only based on 28 days of monitoring, the findings are comparable to the results reported in [39] for a longer period.

The retrieval accuracy in terms of RMSE, ubRMSE, and  $R^2$  was gradually decreased as the spatial resolution became finer for all three downscaling algorithms. For example, for the SMBDA the RMSE value increased from 0.056 to 0.072  $\text{cm}^3/\text{cm}^3$  to 0.092  $\text{cm}^3/\text{cm}^3$  and the  $R^2$  value decreased from 0.76 to 0.60 to 0.44 when the spatial resolution going from 9 to 3 km to 1 km. This result is consistent with the findings in [46], which reported that the accuracy of downscaled brightness temperature reduced as the spatial resolution became finer. This is likely associated with the increased heterogeneity and high level of noise in the radar data. Moreover, it is reasonably expected that the retrieval accuracy would decrease when downscaling the soil moisture to increasingly finer spatial resolution.

The performance of the three downscaling methods differed from each other. The CDM exhibited the poorest performance at all three scales (i.e., 9, 3, and 1 km) with RMSE values ranging from 0.067 to 0.100  $\text{cm}^3/\text{cm}^3$ , while RMSE results for the BTBDA and the SMBDA being much smaller. Since the CDM uses the previous radiometer-scale soil moisture retrieval updated with the moisture change evident in the higher resolution radar backscatter change, the poor performance of the downscaling scheme is likely associated with the accumulating errors from the relatively more noisy radar measurements, which has been pointed out in [30]. The SMBDA presented relatively smaller RMSE and ubRMSE values and higher  $R^2$  values with respect to the BTBDA at 9- and 3-km resolutions.

In order to analyze the influence of  $\Gamma$  on the resulting downscaled soil moisture, the BTBDA and the SMBDA were applied with  $\Gamma = 0$ , with the validation results presented in Table III. By comparing Tables II and III, it can be seen that there was an obvious reduction of RMSE, ubRMSE, and  $R^2$  from using  $\Gamma = 0$  (Table III) to using  $\Gamma \neq 0$  (Table II)

TABLE III  
STATISTICS COMPUTED BETWEEN THE RETRIEVED SOIL MOISTURE AND THE GROUND MEASUREMENTS AT 36-, 9-, 3- AND 1-km RESOLUTIONS;  $N$  IS THE NUMBER OF SAMPLES. THESE RESULTS ARE OBTAINED WITH  $\Gamma = 0$

Scale	Method*	RMSE ( $\text{cm}^3/\text{cm}^3$ )	Bias ( $\text{cm}^3/\text{cm}^3$ )	ubRMSE ( $\text{cm}^3/\text{cm}^3$ )	$R^2$	$N$
9-km	BTBDA	0.064	0.001	0.064	0.67	139
	SMBDA	0.064	0.001	0.064	0.68	140
3-km	BTBDA	0.083	0.005	0.083	0.56	165
	SMBDA	0.080	0.002	0.080	0.57	167
1-km	BTBDA	-	-	-	-	-
	SMBDA	0.107	0.012	0.106	0.37	769

\*: BTBDA and SMBDA represent the Brightness Temperature Based Downscaling Algorithm and the Soil Moisture Based Downscaling Algorithm, respectively. “-”: Data not available due to the lack of 1-km resolution ancillary data for the BTBDA.

for both BTBDA and SMBDA methods at 1-, 3-, and 9-km scales, confirming that the  $\Gamma$  term can be used to compensate the influence of vegetation conditions and help to improve the accuracy of finer resolution soil moisture. In addition, the poor performance of the CDM is likely due in part to not utilizing the  $\Gamma$  term in (4).

It should be mentioned that the size of the Yanco study area was relatively small, thus limiting the number of pixels that could be analyzed. Therefore, more ground measurements are needed to fully evaluate the performance of downscaling algorithms for fusion of Sentinel-1 SAR data and SMAP radiometer data. Moreover, the Yanco study area was dominated by cropping areas and grassland [42]. Since the land cover type is known to affect the performance of the downscaling algorithms [46], more extensive testing of the three algorithms over different land covers is also needed.

#### E. Impact of Incidence Angle Normalization

In order to investigate the influence of incidence angle normalization on the soil moisture retrieval results, 10 differently normalized Sentinel-1  $\sigma^0$  data sets were tested in this paper using a range of discretized  $n$  values (from 0.5 to 5.0 with interval steps of 0.5) in the cosine correction. The range of  $n$  values was wide enough to ensure that it covered all possible  $n$  values for different land cover types in [50]. For each pixel, 10 soil moisture retrieval results were obtained and the maximum difference defined as the difference between the largest and the smallest soil moisture values was calculated. The maximum difference represented the variability in soil moisture retrievals due to  $n$  value.

Fig. 9 displays the cumulative probability distribution of the maximum difference value over the entire study area for all days at three scales (i.e., 9, 3, and 1 km) for the different downscaling algorithms. It can be observed that for all three downscaling algorithms, about 98% pixels had maximum difference value below a threshold value of 0.010  $\text{cm}^3/\text{cm}^3$  at three scales. This result clearly demonstrated that the retrieved soil moisture was almost uninfluenced by the  $n$  value selected for the incidence angle normalization, which agrees well with the finding in [54]. It is also observed that for each

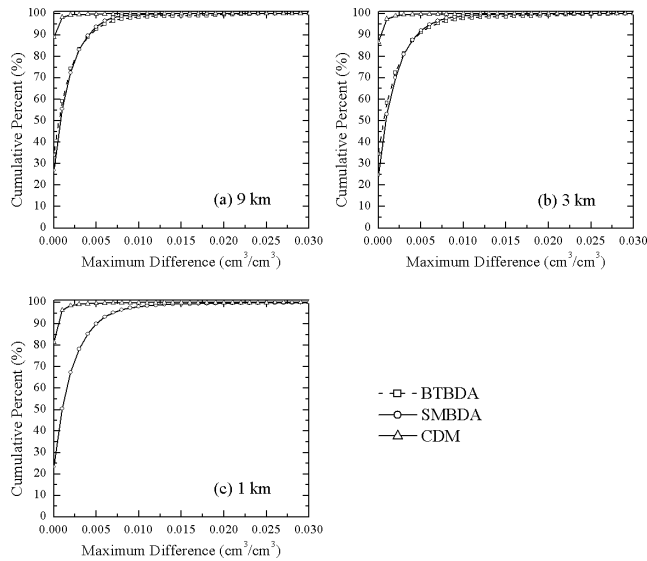


Fig. 9. Cumulative probability distribution of the maximum difference value defined as the difference between the largest and the smallest soil moisture values from different  $n$  values selected for the incidence angle normalization for all days for different downscaling algorithms at (a) 9-, (b) 3-, and (c) 1-km scales. BTBDA, SMBDA, and CDM represent the brightness temperature-based downscaling algorithm, the soil moisture-based downscaling algorithm, and the change detection method, respectively.

downscaling method, the cumulative percent value decreased when the spatial resolution went from 9 to 1 km, indicating that the coarser the spatial resolution, the less influence the incidence angle normalization had on the retrieval accuracy.

Among the three downscaling methods, the CDM was almost unaffected by the incidence angle normalization since almost all pixels had a maximum difference value below  $0.001 \text{ cm}^3/\text{cm}^3$ . This result is not surprising since for each pixel the incidence angle almost remained constant at all Sentinel-1 SAR acquisition dates and the influence of incidence angle on radar backscatter was canceled out through the differencing of radar backscatter. The influences of incidence angle normalization on the BTBDA and SMBDA were very similar since their cumulative distribution functions were very close to each other.

In summary, the accuracy of the downscaling algorithm was almost independent on the choice of  $n$  value selected for incidence angle normalization. However, the incidence angle of Sentinel-1 SAR data was around  $40^\circ$  over the Yanco area so that the validation results in Section IV-D would not be influenced by incidence angle normalization to  $40^\circ$ .

## V. CONCLUSION

This paper provided an extensive analysis of three downscaling algorithms for high-resolution soil moisture estimation using combined Sentinel-1 radar and SMAP radiometer data. These algorithms include the BTBDA (the SMAP baseline algorithm), the SMBDA (the SMAP optional algorithm), and a CDM. The Sentinel-1 SAR data were used to disaggregate the SMAP radiometer data at spatial resolutions of 9, 3, and 1 km over a semiarid landscape in southeastern Australia from May 2015 to May 2016. The downscaled soil moisture was

validated by ground soil moisture measurements collected by a network of 37 individual points in the study area.

The results indicated that the RMSE values of downscaled soil moisture at 9-km resolution were 0.057, 0.056, and  $0.067 \text{ cm}^3/\text{cm}^3$  for the BTBDA, the SMBDA, and the CDM, respectively. The RMSE value of each algorithm generally decreased from 9 to 1 km due to the increased heterogeneity captured from observations at finer spatial scale and the higher noise of the radar observation at finer scale. Among the three downscaling methods tested, the SMBDA showed the best performance in terms of correctly detecting the soil moisture pattern and relatively lower RMSE values. In addition, the SMBDA could generate more spatially complete soil moisture maps compared to the BTBDA. Therefore, the SMBDA is recommended for the combined Sentinel-1 radar and SMAP radiometer setup for soil moisture monitoring.

It was shown that the  $\Gamma$  term can be used to compensate the influence of vegetation conditions to some degree, and the inclusion of  $\Gamma$  can significantly improve the accuracy of the three downscaling algorithms, which is in good agreement with previous findings. This result emphasizes the requirement for cross-polarized SAR data as available from Sentinel-1.

Since Sentinel-1 SAR data are collected at multiple incidence angles within its swath, correction for  $\sigma^0$  differences due to this angular variability is needed. In this paper, the cosine correction was employed and the influence of incidence angle normalization on downscaled soil moisture was investigated. The results demonstrate that the soil moisture downscaling accuracy is not significantly influenced by the  $n$  value selected for the incidence angle normalization.

One limitation for this paper was that the study area was relatively small, limiting the number of pixels that could be analyzed. In addition, the dominant land cover types of the study area were cropland and pasture, making it important to further investigate these downscaling algorithms for a comprehensive range of land surface conditions in future studies.

## ACKNOWLEDGMENT

The authors would like to thank all the fourth SMAP experiment participants. They would also like to thank the reviewers for their very detailed comments that helped improve the quality of this paper.

## REFERENCES

- [1] T. E. Ochsner *et al.*, "State of the art in large-scale soil moisture monitoring," *Soil Sci. Soc. Amer. J.*, vol. 77, no. 6, pp. 1888–1919, 2013.
- [2] E. G. Njoku, T. J. Jackson, V. Lakshmi, T. K. Chan, and S. V. Nghiem, "Soil moisture retrieval from AMSR-E," *IEEE Trans. Geosci. Remote Sens.*, vol. 41, no. 2, pp. 215–229, Feb. 2003.
- [3] Z. Bartalis *et al.*, "Initial soil moisture retrievals from the METOP-A Advanced Scatterometer (ASCAT)," *Geophys. Res. Lett.*, vol. 34, no. 20, p. L20401, Oct. 2007.
- [4] Y. H. Kerr *et al.*, "The SMOS mission: New tool for monitoring key elements of the global water cycle," *Proc. IEEE*, vol. 98, no. 5, pp. 666–687, May 2010.
- [5] D. Entekhabi *et al.*, "The Soil Moisture Active Passive (SMAP) mission," *Proc. IEEE*, vol. 98, no. 5, pp. 704–716, May 2010.
- [6] R. Torres *et al.*, "GMES Sentinel-1 mission," *Remote Sens. Environ.*, vol. 120, pp. 9–24, May 2012.

- [7] J. Leese, T. Jackson, A. Pitman, and P. Dirmeyer, "Meeting summary: GEWEX/BAHC international workshop on soil moisture monitoring, analysis, and prediction for hydrometeorological and hydroclimatological applications," *Bull. Amer. Meteorol. Soc.*, vol. 82, no. 7, pp. 1423–1430, Jul. 2001.
- [8] N. S. Chauhan, S. Miller, and P. Ardanuy, "Spaceborne soil moisture estimation at high resolution: A microwave-optical/IR synergistic approach," *Int. J. Remote Sens.*, vol. 24, no. 22, pp. 4599–4622, 2003.
- [9] M. Piles *et al.*, "Downscaling SMOS-derived soil moisture using MODIS visible/infrared data," *IEEE Trans. Geosci. Remote Sens.*, vol. 49, no. 9, pp. 3156–3166, Sep. 2011.
- [10] M. Choi and Y. Hur, "A microwave-optical/infrared disaggregation for improving spatial representation of soil moisture using AMSR-E and MODIS products," *Remote Sens. Environ.*, vol. 124, pp. 259–269, Sep. 2012.
- [11] M. Piles *et al.*, "A downscaling approach for SMOS land observations: Evaluation of high-resolution soil moisture maps over the Iberian Peninsula," *IEEE J. Sel. Topics Appl. Earth Observ. Remote Sens.*, vol. 7, no. 9, pp. 3845–3857, Sep. 2014.
- [12] S. Sánchez-Ruiz, M. Piles, N. Sánchez, J. Martínez-Fernández, M. Vall-llossera, and A. Camps, "Combining SMOS with visible and near/shortwave/thermal infrared satellite data for high resolution soil moisture estimates," *J. Hydrol.*, vol. 516, pp. 273–283, Aug. 2014.
- [13] M. Piles, G. P. Petropoulos, N. Sánchez, A. González-Zamora, and G. Ireland, "Towards improved spatio-temporal resolution soil moisture retrievals from the synergy of SMOS and MSG SEVIRI spaceborne observations," *Remote Sens. Environ.*, vol. 180, pp. 403–417, Jul. 2016.
- [14] O. Merlin, J. P. Walker, A. Chehbouni, and Y. Kerr, "Towards deterministic downscaling of SMOS soil moisture using MODIS derived soil evaporative efficiency," *Remote Sens. Environ.*, vol. 112, no. 10, pp. 3935–3946, Oct. 2008.
- [15] O. Merlin, A. Al Bitar, J. P. Walker, and Y. Kerr, "A sequential model for disaggregating near-surface soil moisture observations using multi-resolution thermal sensors," *Remote Sens. Environ.*, vol. 113, no. 10, pp. 2275–2284, Oct. 2009.
- [16] O. Merlin, C. Rudiger, A. A. Bitar, P. Richaume, J. P. Walker, and Y. H. Kerr, "Disaggregation of SMOS soil moisture in Southeastern Australia," *IEEE Trans. Geosci. Remote Sens.*, vol. 50, no. 5, pp. 1556–1571, May 2012.
- [17] N. Djamali, R. Magagi, K. Goita, O. Merlin, Y. Kerr, and A. Walker, "Disaggregation of SMOS soil moisture over the Canadian Prairies," *Remote Sens. Environ.*, vol. 170, pp. 255–268, Dec. 2015.
- [18] Y. Malbêteau, O. Merlin, B. Molero, C. Rüdiger, and S. Bacon, "DISPATCH as a tool to evaluate coarse-scale remotely sensed soil moisture using localized *in situ* measurements: Application to SMOS and AMSR-E data in Southeastern Australia," *Int. J. Appl. Earth Observ. Geoinf.*, vol. 45, pp. 221–234, Mar. 2016.
- [19] B. Molero *et al.*, "SMOS disaggregated soil moisture product at 1 km resolution: Processor overview and first validation results," *Remote Sens. Environ.*, vol. 180, pp. 361–376, Jul. 2016.
- [20] J. G. Liu, "Smoothing filter-based intensity modulation: A spectral preserve image fusion technique for improving spatial details," *Int. J. Remote Sens.*, vol. 21, no. 18, pp. 3461–3472, Nov. 2000.
- [21] J. Kim and T. S. Hogue, "Improving spatial soil moisture representation through integration of AMSR-E and MODIS products," *IEEE Trans. Geosci. Remote Sens.*, vol. 50, no. 2, pp. 446–460, Feb. 2012.
- [22] J. Peng, J. Niesel, and A. Loew, "Evaluation of soil moisture downscaling using a simple thermal-based proxy—The REMEDHUS network (Spain) example," *Hydrol. Earth Syst. Sci.*, vol. 19, no. 12, pp. 4765–4782, 2015.
- [23] J. Peng, A. Loew, S. Zhang, J. Wang, and J. Niesel, "Spatial downscaling of satellite soil moisture data using a vegetation temperature condition index," *IEEE Trans. Geosci. Remote Sens.*, vol. 54, no. 1, pp. 558–566, Jan. 2016.
- [24] N. Djamali, R. Magagi, K. Goita, O. Merlin, Y. Kerr, and A. Roy, "A combination of DISPATCH downscaling algorithm with CLASS land surface scheme for soil moisture estimation at fine scale during cloudy days," *Remote Sens. Environ.*, vol. 184, pp. 1–14, Oct. 2016.
- [25] E. G. Njoku *et al.*, "Observations of soil moisture using a passive and active low-frequency microwave airborne sensor during SGP99," *IEEE Trans. Geosci. Remote Sens.*, vol. 40, no. 12, pp. 2659–2673, Dec. 2002.
- [26] N. N. Das, D. Entekhabi, E. G. Njoku, J. J. C. Shi, J. T. Johnson, and A. Colliander, "Tests of the SMAP combined radar and radiometer algorithm using airborne field campaign observations and simulated data," *IEEE Trans. Geosci. Remote Sens.*, vol. 52, no. 4, pp. 2018–2028, Apr. 2014.
- [27] N. N. Das, D. Entekhabi, and E. G. Njoku, "An algorithm for merging SMAP radiometer and radar data for high-resolution soil-moisture retrieval," *IEEE Trans. Geosci. Remote Sens.*, vol. 49, no. 5, pp. 1504–1512, May 2011.
- [28] U. Narayan, V. Lakshmi, and T. J. Jackson, "High-resolution change estimation of soil moisture using L-band radiometer and Radar observations made during the SMEX02 experiments," *IEEE Trans. Geosci. Remote Sens.*, vol. 44, no. 6, pp. 1545–1554, Jun. 2006.
- [29] U. Narayan and V. Lakshmi, "Characterizing subpixel variability of low resolution radiometer derived soil moisture using high resolution radar data," *Water Resour. Res.*, vol. 44, no. 6, p. W06425, 2008.
- [30] M. Piles, D. Entekhabi, and A. Camps, "A change detection algorithm for retrieving high-resolution soil moisture from SMAP radar and radiometer observations," *IEEE Trans. Geosci. Remote Sens.*, vol. 47, no. 12, pp. 4125–4131, Dec. 2009.
- [31] X. Zhan, P. R. Houser, J. P. Walker, and W. T. Crow, "A method for retrieving high-resolution surface soil moisture from hydros L-band radiometer and Radar observations," *IEEE Trans. Geosci. Remote Sens.*, vol. 44, no. 6, pp. 1534–1544, Jun. 2006.
- [32] X. Wu, J. P. Walker, N. N. Das, R. Panciera, and C. Rüdiger, "Evaluation of the SMAP brightness temperature downscaling algorithm using active-passive microwave observations," *Remote Sens. Environ.*, vol. 155, pp. 210–221, Dec. 2014.
- [33] C. Montzka *et al.*, "Investigation of SMAP fusion algorithms with airborne active and passive L-band microwave remote sensing," *IEEE Trans. Geosci. Remote Sens.*, vol. 54, no. 7, pp. 3878–3889, Jul. 2016.
- [34] X. Wu, J. P. Walker, C. Rüdiger, R. Panciera, and Y. Gao, "Inter-comparison of alternate soil moisture downscaling algorithms using active-passive microwave observations," *IEEE Geosci. Remote Sens. Lett.*, vol. 14, no. 2, pp. 179–183, Feb. 2017.
- [35] S. Yueh, D. Entekhabi, P. O'Neill, E. Njoku, and J. Entin, "NASA Soil Moisture Active Passive mission status and science performance," in *Proc. IEEE Int. Geosci. Remote Sens. Symp.*, Jul. 2016, pp. 116–119.
- [36] C. Rüdiger, C.-H. Su, D. Ryu, and W. Wagner, "Disaggregation of low-resolution L-band radiometry using C-band radar data," *IEEE Geosci. Remote Sens. Lett.*, vol. 13, no. 10, pp. 1425–1429, Oct. 2016.
- [37] E. Santi, S. Paloscia, S. Pettinato, D. Entekhabi, S. H. Alemohammad, and A. G. Konings, "Integration of passive and active microwave data from SMAP, AMSR2 and Sentinel-1 for Soil Moisture monitoring," in *Proc. IEEE Int. Geosci. Remote Sens. Symp.*, Jul. 2016, pp. 5252–5255.
- [38] N. N. Das, D. Entekhabi, S. Kim, S. Yueh, and P. O'Neill, "Combining SMAP and Sentinel data for high-resolution Soil Moisture product," in *Proc. IEEE Int. Geosci. Remote Sens. Symp.*, Jul. 2016, pp. 129–131.
- [39] S. K. Chan *et al.*, "Assessment of the SMAP passive soil moisture product," *IEEE Trans. Geosci. Remote Sens.*, vol. 54, no. 8, pp. 4994–5007, Aug. 2016.
- [40] A. Colliander *et al.*, "Validation of SMAP surface soil moisture products with core validation sites," *Remote Sens. Environ.*, vol. 191, pp. 215–231, Mar. 2017.
- [41] A. B. Smith *et al.*, "The Murrumbidgee soil moisture monitoring network data set," *Water Resour. Res.*, vol. 48, no. 7, p. W07701, 2012.
- [42] R. Panciera *et al.*, "The soil moisture active passive experiments (SMAPEx): Toward soil moisture retrieval from the SMAP mission," *IEEE Trans. Geosci. Remote Sens.*, vol. 52, no. 1, pp. 490–507, Jan. 2014.
- [43] K. Didan. (2015). *MOD13A2 MODIS/Terra Vegetation Indices 16-Day L3 Global 1km SIN Grid V006. NASA EOSDIS Land Processes DAAC*. [Online]. Available: <https://doi.org/10.5067/modis/mod13a2.006>
- [44] P. O'Neill, S. Chan, E. Njoku, T. Jackson, and R. Bindlish. *Algorithm Theoretical Basis Document: Level 2 & 3 Soil Moisture (Passive) Data Products, Revision B*. Accessed: 2017. [Online]. Available: [https://smap.jpl.nasa.gov/system/internal\\_resources/details/original/316\\_L2\\_SM\\_P\\_ATBD\\_v7\\_Sep2015.pdf](https://smap.jpl.nasa.gov/system/internal_resources/details/original/316_L2_SM_P_ATBD_v7_Sep2015.pdf)
- [45] I. E. Mladenova, T. J. Jackson, R. Bindlish, and S. Hensley, "Incidence angle normalization of radar backscatter data," *IEEE Trans. Geosci. Remote Sens.*, vol. 51, no. 3, pp. 1791–1804, Mar. 2013.
- [46] X. Wu, J. P. Walker, C. Rüdiger, and R. Panciera, "Effect of land-cover type on the SMAP active/passive soil moisture downscaling algorithm performance," *IEEE Geosci. Remote Sens. Lett.*, vol. 12, no. 4, pp. 846–850, Apr. 2015.
- [47] D. J. Leroux *et al.*, "Active-passive disaggregation of brightness temperatures during the SMAPVEX12 campaign," *IEEE Trans. Geosci. Remote Sens.*, vol. 54, no. 12, pp. 6859–6867, Dec. 2016.

- [48] N. N. Das, D. Entekhabi, R. S. Dunbar, E. G. Njoku, and S. H. Yueh, "Uncertainty estimates in the SMAP combined active-passive downscaled brightness temperature," *IEEE Trans. Geosci. Remote Sens.*, vol. 54, no. 2, pp. 640–650, Feb. 2016.
- [49] T. J. Jackson, "Measuring surface soil moisture using passive microwave remote sensing," *Hydrol. Process.*, vol. 7, no. 2, pp. 139–152, Apr./Jun. 1993.
- [50] J. P. Ardila, V. Tolpekin, and W. Bijker, "Angular backscatter variation in L-band ALOS ScanSAR images of tropical forest areas," *IEEE Geosci. Remote Sens. Lett.*, vol. 7, no. 4, pp. 821–825, Oct. 2010.
- [51] N. Ye, J. P. Walker, and C. Rüdiger, "A cumulative distribution function method for normalizing variable-angle microwave observations," *IEEE Trans. Geosci. Remote Sens.*, vol. 53, no. 7, pp. 3906–3916, Jul. 2015.
- [52] F. T. Ulaby, R. K. Moore, and A. K. Fung, *Microwave Remote Sensing: Microwave Remote Sensing Fundamentals and Radiometry*, vol. 2. Reading, MA, USA: Addison-Wesley, 1981.
- [53] C. H. Menges, J. J. Van Zyl, G. J. E. Hill, and W. Ahmad, "A procedure for the correction of the effect of variation in incidence angle on AIRSAR data," *Int. J. Remote Sens.*, vol. 22, no. 5, pp. 829–841, 2001.
- [54] R. V. D. Velde, M. S. Salama, O. A. Eweys, J. Wen, and Q. Wang, "Soil moisture mapping using combined active/passive microwave observations over the east of The Netherlands," *IEEE J. Sel. Topics Appl. Earth Observ. Remote Sens.*, vol. 8, no. 9, pp. 4355–4372, Sep. 2015.
- [55] F. T. Ulaby, R. K. Moore, and A. K. Fung, *Microwave Remote Sensing: Active and Passive: From Theory to Applications*, vol. 3. Reading, MA, USA: Addison-Wesley, 1981.
- [56] A. K. Fung, *Microwave Scattering and Emission Models and Their Applications*. Norwood, MA, USA: Artech House, 1994.



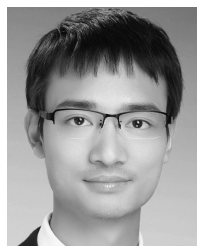
**Xiaoling Wu** received the B.E. degree in biomedical engineering from Zhejiang University, Hangzhou, China, in 2009, and the Ph.D. degree in civil engineering from Monash University, Melbourne, VIC, Australia, in 2015. Her B.E. thesis focused on the development of biosensor using nanomaterial. Her Ph.D. thesis focused on the downscaling of soil moisture using airborne radar and radiometer observations in order to provide an accurate and high-resolution (better than 10km) soil moisture product with potential benefit in the areas of weather forecasting, flood and drought prediction, and agricultural activities.

She did one-year research in computer science at the University of Copenhagen, Copenhagen, Denmark, in 2010. She is currently a Research Fellow with Monash University and continuing high-resolution soil moisture work. Her research interests include microwave remote sensing of soil moisture, soil moisture downscaling, and proximal soil moisture sensing for real-time agricultural applications.



**Nan Ye** received the B.E. degree in hydraulic and hydropower engineering from Tsinghua University, Beijing, China, in 2006, and the Ph.D. degree in civil engineering from Monash University, Melbourne, Australia, in 2014.

In 2013, he joined the Department of Geographic Information Science, Nanjing University, Nanjing, China, where he was involved in snow properties' retrievals from optical and SAR data. In 2014, he returned to Monash University where he coordinated a number of airborne field experiments for the in-orbit calibration/validation of the Soil Moisture Active Passive mission in the Murrumbidgee river catchment, southeast of Australia. He is currently a Senior Research Fellow with Monash University, focusing on P-band passive microwave remote sensing of soil moisture.



**Lian He** received the B.S. degree in remote sensing science and technology from Wuhan University, Wuhan, China, in 2010, and the Ph.D. degree in cartology and geography information system from Peking University, Beijing, China, in 2016.

From 2013 to 2014, he was a Visiting Research Student with the Department of Civil Engineering, Monash University, Melbourne, VIC, Australia. He is currently a Post-Doctoral Fellow with the Department of Hydraulic Engineering, Tsinghua University, Beijing. His research interests include

microwave remote sensing of soil moisture and soil moisture downscaling.



**Jeffrey P. Walker** received the B.E. (civil) and B.Surveying degrees (with Hons. and University Medal) and the Ph.D. degree in water resources engineering from The University of Newcastle, Callaghan, NSW, Australia, in 1995 and 1999, respectively. His Ph.D. thesis was among the early pioneering research on estimation of root-zone soil moisture from assimilation of remotely sensed surface soil moisture observations.

He was with the NASA Goddard Space Flight Center, Greenbelt, MD, USA, to implement his soil moisture work globally. In 2001, he joined the Department of Civil and Environmental Engineering, University of Melbourne, Parkville, VIC, Australia, as a Lecturer, where he continued his soil moisture work, including the development of the only Australian airborne capability for simulating new satellite missions for soil moisture. In 2010, he was appointed as Professor at the Department of Civil Engineering, Monash University, Melbourne, VIC, Australia, where he is continuing this research. He is contributing to soil moisture satellite missions at NASA, ESA, and JAXA, as a Science Team Member for the Soil Moisture Active Passive mission and a Cal/val Team Member for the Soil Moisture and Ocean Salinity and Global Change Observation Mission—Water, respectively.



**Yang Hong** received the B.S. degree from the School of Earth and Space Sciences, Peking University, Beijing, China, in 1996, the M.S. degree from the College of Urban and Environmental Sciences, Peking University, in 1999, and the Ph.D. degree from the Department of Hydrology and Water Resources, College of Engineering, The University of Arizona, Tucson, AZ, USA, in 2003.

He is currently the Gallogly Chair Professor with The University of Oklahoma, Norman, OK, USA, and also a Lecture Professor with the Institute of

Remote Sensing and GIS, Peking University, and also with the Department of Hydraulic Engineering, Tsinghua University, Beijing. His research interests include radar/satellite remote sensing of water cycle, hydrology and water resource, hydrometeorology, and geographic information science.



**Xiaona Chen** received the M.S. degree in cartography and geography information system from the Chinese Academy of Sciences, Beijing, China, in 2010, and the Ph.D. degree in cartography and geography information system from Beijing Normal University, Beijing, in 2016.

She is currently a Post-Doctoral Fellow with the Department of Hydraulic Engineering, Tsinghua University, Beijing. Her research interests include climate change, cryosphere, remote sensing, and snow cover.

Dr. Chen is a member of the American Geophysical Union.